Photonics and Nanostructures - Fundamentals and Applications 36 (2019) 100726

Contents lists available at ScienceDirect

Photonics and Nanostructures - Fundamentals and Applications

journal homepage: www.elsevier.com/locate/photonics

Enhancement of efficiency of second-harmonic generation from MoS_2 monolayers in 1D Fibonacci photonic crystals

F. Asadollah Zarif, M. Khazaei Nezhad*, H. Rastegrar Moghaddam Rezaieun

Department of Physics, Faculty of Sciences, Ferdowsi University of Mashhad, Mashhad, Iran

ARTICLE INFO

Keywords:
MoS_2 monolayer
Second-harmonic generation
Fibonacci photonic crystal
Bragg mirror

ABSTRACT

In this article, the increase of the efficiency of second-harmonic generation (SHG) from MoS_2 monolayers embedded in different one-dimensional Fibonacci photonic crystal structures is investigated. The systems contain ZnS, SiO_2, and MoS_2 layers with the same thickness of ZnS and SiO_2 films, which are arranged on the basis of different Fibonacci sequences. The transfer matrix method is used to calculate the forward and backward SHG efficiencies in the undepleted pump approximation. The thicknesses of the ZnS and SiO_2 films are changed to obtain the maximum frequency conversion in different structures. Tuning the thicknesses causes the second-harmonic waves generated in each MoS_2 monolayer to interfere constructively. Also, the fundamental and second-harmonic wavelengths are both located at the photonic band gap edges, where the density of electromagnetic modes and the nonlinear interaction time are enhanced. Our results show that the SHG efficiencies were increased in quasiperiodic photonic crystals with respect to the periodic structure with the same number of MoS_2 layers. In Fibonacci photonic crystal structures there are more geometrical parameters that can be tuned to obtain the highest efficiencies. Furthermore, we used a Bragg mirror at one side of each structure to control the propagation direction of the generated second-harmonic waves and to decrease the backward waves, which led to enhancement of the forward waves.

1. Introduction

Two-dimensional (2D) transition metal dichalcogenides (TMDs) exhibit enriched electrical and optical properties, which have attracted much attention in recent years [1–6]. The materials contain one transition metal atom such as molybdenum or tungsten sandwiched between two chalcogen atoms such as sulfur, selenium, and tellurium in a hexagonal structure [1,5–9]. Two-dimensional monolayers of TMDs behave similarly to semiconductors with a direct band gap without crystalline inversion symmetry [6,9–12]. In the absence of inversion symmetry, second-order nonlinear optical effects such as second-harmonic (SH) generation (SHG) are enhanced [9–12]. Dependent on the fabrication methods, for instance, mechanical exfoliation, the second-order susceptibility ($\chi^{(2)}$) can be increased up to 10^{-7} m/V [11–13]. One of the most investigated TMDs is molybdenum disulfide (MoS_2) as a monolayer [3,4,8,10,12–18]. A few layers of MoS_2 show excellent linear and nonlinear optical effects, such as strong photoluminescence and saturable absorption [1,3,4]. Also, the radiation of SH waves from MoS_2 monolayers was observed recently when such monolayers were subjected to Ti:sapphire laser irradiation [10,12–15].

Despite the increased second-order nonlinear optical coefficient in 2D TMDs with respect to the bulk state, an insignificant thickness (about 0.65 nm) diminishes the SHG efficiency in comparison with popular nonlinear crystals such as potassium dihydrogen phosphate, barium borate, and strontium barium niobate. There are some mechanisms to enhance the efficiency of SHG from 2D TMDs such as using them in a microcavity and periodic photonic crystals and excitation at exciton resonances [9,19,20]. Furthermore, aperiodic and quasiperiodic photonic crystals such as those of the Cantor, Thue-Morse, and Fibonacci types show fascinating optical properties [21–23]. In these types of photonic crystals there are several structural parameters that can be tuned to achieve a desirable optical response [22,23].

In this article, we theoretically investigate the increase of the efficiency of SHG from different Fibonacci photonic crystal (FPC) structures in the form of S_i with $i = 2, 3, 4, 5$, where S_i represents different Fibonacci sequences, and with periodicity N. Our FPC structures contain ZnS, SiO_2, and MoS_2 layers arranged on the basis of different Fibonacci sequences. We concentrate on the phase matching of SH waves generated from different MoS_2 layers by tuning the thickness of the dielectric materials between them that are used in different structures. The study was done by the transfer matrix method [24–27]. Our results show that the SHG efficiencies are increased in FPCs with

* Corresponding author.
E-mail address: khazaeinezhad@um.ac.ir (M.K. Nezhad).

https://doi.org/10.1016/j.photonics.2019.100726
Received 30 December 2018; Received in revised form 24 April 2019; Accepted 9 July 2019
Available online 31 July 2019

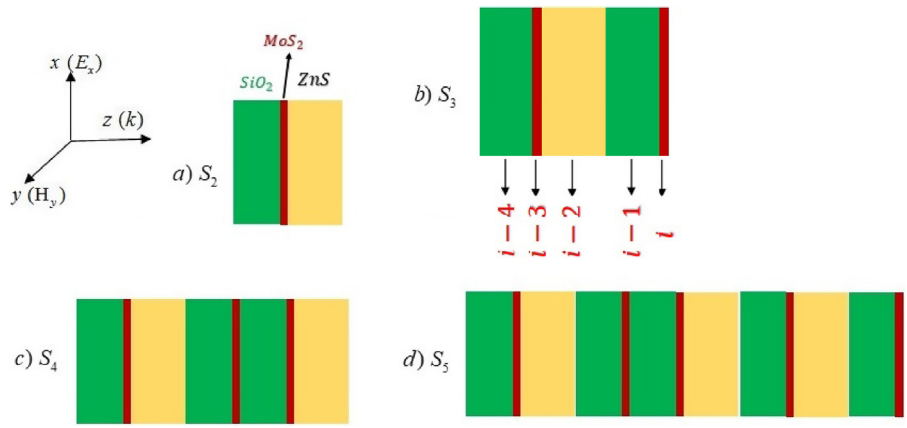

Fig. 1. Building blocks of different Fibonacci photonic crystals: (a) S_2, (b) S_3, (c) S_4, and (d) S_5.

respect to the periodic structure with the same number of MoS_2 layers. Moreover, we used a Bragg mirror at one side of the FPCs to decrease the backward SH waves and to enhance the forward ones. We hope these structures can be used as a component of nanophotonic circuits and nonlinear light sources.

This article is organized as follows. In Section 2, the one-dimensional (1D) photonic crystal structures and the transfer matrix method are introduced. Numerical results and a discussion are presented in Section 3. Finally, we summarize our results in Section 4.

2. Theoretical model

In a Fibonacci sequence the nth term (S_n) is obtained from the two previous terms following the recurrence relation $S_{n+1} = S_n S_{n-1}$. As reported in many experimental studies, MoS_2 monolayers are deposited on SiO_2 and ZnS substrates [4,10,12–14,16–18,31]. Therefore, we used S_0 = ZnS layer and $S_1 = SiO_2/MoS_2$ bilayers in our structures. The building blocks of the S_i (i = 2, 3, 4, 5) FPCs used in our simulations are shown in Fig. 1.

The complex relative electric permittivity of MoS_2 monolayers is well defined here by the hybrid Lorentz–Drude–Gaussian model with six resonances as $\varepsilon_M = \varepsilon_M^{\mathrm{LD}} + \varepsilon_M^{G}$ [16–18]. The Lorentz–Drude part of the MoS_2 electric permittivity is given by [16–18]

$$\varepsilon_M^{\mathrm{LD}}(\omega) = \varepsilon_\infty + \sum_{j=0}^{5} \frac{S_j \omega_P^2}{\omega_j^2 - \omega^2 - i\Gamma_j \omega}, \tag{1}$$

where ω_j, S_j, and Γ_j are the resonance frequency, oscillator strength, and damping coefficient of the jth resonance, respectively. The values of these parameters are given in Table 1. Also, ω_P, the plasma frequency of the MoS_2 layer is $\frac{28.3}{2\pi}$ meV and ε_∞, the background or DC permittivity, is 4.44 [16–18].

The Gaussian part of the MoS_2 electric permittivity contains imaginary and real terms. The imaginary term is as follows [16]:

$$\varepsilon_{\mathrm{iM}}^{G}(\omega) = \varepsilon_I \exp\left(-\frac{(\hbar\omega - E)^2}{2\sigma^2}\right), \tag{2}$$

Table 1
Resonance strength, damping coefficient, and resonance frequency for the Lorentz–Drude part of the MoS_2 electric permittivity [16].

j	ω_j (eV)	Γ_j (eV)	S_j
0	0	1.0853×10^{-2}	2.0089×10^{5}
1	1.88	5.9099×10^{-2}	5.7534×10^{4}
2	2.03	1.1302×10^{-1}	8.1496×10^{4}
3	2.78	1.1957×10^{-1}	8.2293×10^{4}
4	2.91	2.8322×10^{-1}	3.3130×10^{5}
5	4.31	7.8515×10^{-1}	4.3906×10^{6}

where $\varepsilon_I = 23.224$, $E = 2.7723$ eV, and $\sigma = 0.3089$ eV. By application of the Kramers–Kronig dispersion relation, the real part of the Gaussian component of the MoS_2 electric permittivity can be calculated as [16]

$$\varepsilon_{\mathrm{rM}}^{G}(\omega) = 1 + \frac{1}{\pi} P.\,V. \int_{-\infty}^{\infty} \frac{\varepsilon_{\mathrm{iM}}^{G}(\omega')}{(\omega' - \omega)} d\omega', \tag{3}$$

which leads to

$$\varepsilon_{\mathrm{rM}}^{G}(\omega) = 1 - \frac{2\varepsilon_I}{\sqrt{\pi}} \mathrm{DF}\left(\frac{(\hbar\omega - E)}{\sqrt{2}\sigma}\right), \tag{4}$$

where $DF(x)$ is the Dawson function of argument x. The refractive index and extinction coefficient of the MoS_2 monolayer are obtained from the overall complex electric permittivity as follows:

$$n_M(\omega) = \sqrt{\frac{1}{2}(\varepsilon_{\mathrm{rM}} + \sqrt{\varepsilon_{\mathrm{rM}}^2 + \varepsilon_{\mathrm{iM}}^2})},$$
$$K_M(\omega) = \sqrt{\frac{1}{2}(-\varepsilon_{\mathrm{rM}} + \sqrt{\varepsilon_{\mathrm{rM}}^2 + \varepsilon_{\mathrm{iM}}^2})}. \tag{5}$$

The refractive indices of the SiO_2 and ZnS films are obtained, respectively, as [29,30]

$$n_S(\lambda) = \sqrt{A_S + \frac{B_S \lambda^2}{\lambda^2 - C_S^2} + \frac{D_S \lambda^2}{\lambda^2 - E_S^2}}, \tag{6}$$

where $A_S = 1.28604141$, $B_S = 1.07044083$, $C_S = 0.10029$, $D_S = 1.10202242$, and $E_S = 10$, and

$$n_Z(\lambda) = \sqrt{A_Z + \frac{B_Z}{\lambda^2 - C_Z^2} + \frac{D_Z}{\lambda^2 - E_Z^2}}, \tag{7}$$

where $A_Z = 8.393$, $B_Z = 0.14383$, $C_Z = 0.2421$, $D_Z = 4430.99$, and $E_Z = 36.72$. In Eqs. (6) and (7) λ has the unit of micrometers. Moreover, the refractive index of surrounding air was set to 1.

The interface of the whole 1D FPC components is assumed to lie in the xy plane (see Fig. 1). The fundamental wave (FW) of wavelength λ and with electric field polarization along the x-axis is incident normally on the 1D nonlinear photonic crystal (NPC) in the z direction.

A MoS_2 crystal has D_{3h} symmetry, having a hexagonal structure with the following nonzero element of the second-order nonlinear susceptibility tensor [10]: $\chi^{(2)}_{y'y'y'} = -\chi^{(2)}_{y'x'x'} = -\chi^{(2)}_{x'x'y'} = -\chi^{(2)}_{x'y'x'}$ where x', y', z' are crystalline coordinates. Here x' is along the armchair direction (see Fig. 2). The incident beam is linearly polarized along the x direction in our structures, where the x, y, and z directions are shown in Fig. 1 and are known as laboratory coordinates. If θ is the angle between the incident electric field (x) and the armchair direction of MoS_2 monolayers (x'), then it was shown that the parallel (x) and perpendicular (y) components of the SH electric field are proportional to $\sin 3\theta$ and $\cos 3\theta$, respectively [10]. Therefore, the SH electric field has only a parallel component if $\theta = 30$ is adjusted by rotation of the incident

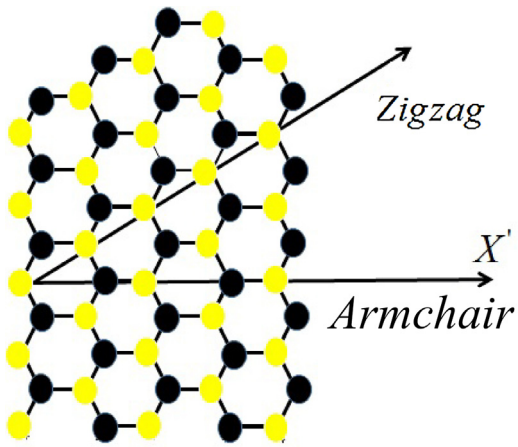

Fig. 2. The lattice structure of the MoS_2 monolayer. Black circles represent sulfur atoms and yellow circles represent molybdenum atoms [20]. (For interpretation of the references to color in this figure legend, the reader is referred to the web version of this article.)

light polarization, and, what is more, the scalar equation with an effective susceptibility for the generated SH wave can be applied.

In the undepleted pump or small signal approximation, where back-conversion of the SH wave to the FW is negligible, the FW electric field $E_i^{(1)}(z)$ and the SH electric field $E_i^{(2)}(z)$ in the ith layer satisfy the following equations [24–27]:

$$\frac{d^2E_i^{(1)}(z)}{dz^2} + k_i^{(1)2}E_i^{(1)}(z) = 0, \tag{8}$$

$$\frac{d^2E_i^{(2)}(z)}{dz^2} + k_i^{(2)2}E_i^{(2)}(z) = -k_{20}^2\chi_i^{(2)}E_i^{(1)2}(z), \tag{9}$$

where $\chi_i^{(2)}$ is the second-order nonlinear optical coefficient of the ith layer and $k_i^{(1)} = n_i^{(1)}k_{10}$, $k_i^{(2)} = n_i^{(2)}k_{20}$, $k_{20} = 2k_{10}$, and $k_{10} = \frac{\omega}{c}$, where $n_i^{(1)}$ and $n_i^{(2)}$ are the refractive indices of the ith layer material at the FW frequency and the SH frequency, respectively, and c is the speed of light in a vacuum.

On the basis of Eq. (8), the FW electric field in the ith layer can be expanded with forward and backward plane waves that propagate in the z direction as follows:

$$E_i^{(1)}(z) = a_i^{(1)}e^{ik_i^{(1)}(z-z_{i-1})} + b_i^{(1)}e^{-ik_i^{(1)}(z-z_{i-1})}, \tag{10}$$

where $a_i^{(1)}$ and $b_i^{(1)}$ are the forward and backward FW electric field amplitudes at the beginning of the ith layer, respectively, and $z_i = z_{i-1} + d_i$ (z_0 is set to zero), where d_i is the thickness of the ith layer. By using the continuous conditions of electric and magnetic fields at each interface, we obtain

$$\begin{pmatrix} a_i^{(1)} \\ b_i^{(1)} \end{pmatrix} = t_i^{(1)}\begin{pmatrix} a_{i-1}^{(1)} \\ b_{i-1}^{(1)} \end{pmatrix}, \tag{11}$$

where $t_i^{(1)}$ is defined as [26]

$$t_i^{(1)} = D_0^{-1}D_iP_iD_i^{-1}D_0, \tag{12}$$

where the related matrices are

$$D_0 = \begin{pmatrix} 1 & 1 \\ n_0 & -n_0 \end{pmatrix}, \quad D_i = \begin{pmatrix} 1 & 1 \\ n_i^{(1)} & -n_i^{(1)} \end{pmatrix}, \quad P_i = \begin{pmatrix} e^{ik_i^{(1)}d_i} & 0 \\ 0 & e^{-ik_i^{(1)}d_i} \end{pmatrix}. \tag{13}$$

In the matrix D_0, n_0 is the air background refractive index and is set to 1. The overall transfer matrix (T) of the system, calculated by successive products of the individual transfer matrix t_i, can be used to connect the FW electric field amplitude on the left side and the right side of the structure as [24–27]

$$\begin{pmatrix} E_t^{(1)} \\ 0 \end{pmatrix} = T\begin{pmatrix} E_0 \\ E_r^{(1)} \end{pmatrix}. \tag{14}$$

The reflected and transmitted FW electric field amplitudes are obtained as $E_r^{(1)} = -\frac{T_{21}}{T_{22}}E_0$ and $E_t^{(1)} = \frac{|T|}{T_{22}}E_0$, respectively, with $|T|$ the determinant of the overall transfer matrix T. Furthermore, starting from E_0 and $E_r^{(1)}$ and applying the recursion algorithm, one can thoroughly determine the forward ($a_i^{(1)}$) and backward ($b_i^{(1)}$) FW electric field amplitudes of each layer. For instance, in the S_3 structure with five components in its building block (see Fig. 1), we obtained the following relations:

$$\begin{aligned}
\begin{pmatrix} a_{5i-4}^{(1)} \\ b_{5i-4}^{(1)} \end{pmatrix} &= D_S^{-1}t^{i-1}D_0\begin{pmatrix} E_0 \\ E_r^{(1)} \end{pmatrix}, \\
\begin{pmatrix} a_{5i-3}^{(1)} \\ b_{5i-3}^{(1)} \end{pmatrix} &= D_M^{-1}(D_SP_SD_S^{-1})t^{i-1}D_0\begin{pmatrix} E_0 \\ E_r^{(1)} \end{pmatrix}, \\
\begin{pmatrix} a_{5i-2}^{(1)} \\ b_{5i-2}^{(1)} \end{pmatrix} &= D_Z^{-1}(D_MP_MD_M^{-1})(D_SP_SD_S^{-1})t^{i-1}D_0\begin{pmatrix} E_0 \\ E_r^{(1)} \end{pmatrix}, \\
\begin{pmatrix} a_{5i-1}^{(1)} \\ b_{5i-1}^{(1)} \end{pmatrix} &= D_S^{-1}(D_ZP_ZD_Z^{-1})(D_MP_MD_M^{-1})(D_SP_SD_S^{-1})t^{i-1}D_0\begin{pmatrix} E_0 \\ E_r^{(1)} \end{pmatrix}, \\
\begin{pmatrix} a_{5i}^{(1)} \\ b_{5i}^{(1)} \end{pmatrix} &= D_M^{-1}(D_SP_SD_S^{-1})(D_ZP_ZD_Z^{-1})(D_MP_MD_M^{-1})(D_SP_SD_S^{-1})t^{i-1}D_0\begin{pmatrix} E_0 \\ E_r^{(1)} \end{pmatrix}.
\end{aligned} \tag{15}$$

$a_{5i-k}^{(1)}$ and $b_{5i-k}^{(1)}$ with $k = 0, 1, 2, 3, 4$ denote the forward and backward FW electric field amplitudes, respectively, at the left-hand side of MoS_2 ($k = 0$), SiO_2 ($k = 1$), ZnS ($k = 2$), MoS_2 ($k = 3$), and SiO_2 ($k = 4$) films in the ith segment (see Fig. 1). The subindexes Z, S, M, and 0 refer to ZnS, SiO_2, MoS_2, and the background medium, respectively. t is the one-segment transfer matrix and is obtained from

$$t = (D_MP_MD_M^{-1})(D_SP_SD_S^{-1})(D_ZP_ZD_Z^{-1})(D_MP_MD_M^{-1})(D_SP_SD_S^{-1}).$$

After calculating the FWs in each layer, we can investigate the generation and propagation of SH waves in our structures. The FW acts as the source of the SH wave (see Eq. (8)). Inserting the FW solution (Eq. (9)) into Eq. (8), we can obtain the SH electric field amplitude in the ith layer as follows:

$$\begin{aligned}
E_i^{(2)}(z) &= a_i^{(2)}e^{ik_i^{(2)}(z-z_{i-1})} + b_i^{(2)}e^{-ik_i^{(2)}(z-z_{i-1})} + A_i[a_i^{(1)}]^2e^{2ik_i^{(1)}(z-z_{i-1})} \\
&\quad + A_i[b_i^{(1)}]^2e^{-2ik_i^{(1)}(z-z_{i-1})} + C_ia_i^{(1)}b_i^{(1)},
\end{aligned} \tag{16}$$

where $a_i^{(2)}$ and $b_i^{(2)}$ are the forward and backward SH electric field amplitudes, respectively, at the beginning of the ith layer, $A_i = -\frac{k_{20}^2\chi_i^{(2)}}{(k_i^{(2)2} - 4k_i^{(1)2})}$, and $C_i = -\frac{2k_{20}^2\chi_i^{(2)}}{k_i^{(2)2}}$ [24–27].

Applying Maxwell's equation as $\vec{\nabla} \times \vec{E}_i^{(2)}(z) = ik_{20}\vec{H}_i^{(2)}(z)$, we can write the SH magnetic field as

$$\begin{aligned}
H_i^{(2)}(z) &= n_i^{(2)}(a_i^{(2)}e^{ik_i^{(2)}(z-z_{i-1})} - b_i^{(2)}e^{-ik_i^{(2)}(z-z_{i-1})}) \\
&\quad + n_i^{(1)}(A_i[a_i^{(1)}]^2e^{2ik_i^{(1)}(z-z_{i-1})} - A_i[b_i^{(1)}]^2e^{-2ik_i^{(1)}(z-z_{i-1})}).
\end{aligned} \tag{17}$$

The forward and backward SH electric field amplitudes at the ith layer and the $(i-1)$th layer are connected through the continuous conditions as follows [24–27]:

$$\begin{pmatrix} a_i^{(2)} \\ b_i^{(2)} \end{pmatrix} = t_i^{(2)}\begin{pmatrix} a_{i-1}^{(2)} \\ b_{i-1}^{(2)} \end{pmatrix} + \begin{pmatrix} r_i^+ \\ r_i^- \end{pmatrix}. \tag{18}$$

The matrices applied are given by [24–27]

$$t_i^{(2)} = G_0^{-1} N_i G_0, \quad N_i = G_i Q_i G_i^{-1},$$
$$\begin{pmatrix} r_i^+ \\ r_i^- \end{pmatrix} = G_0^{-1}[(B_i F_i - N_i B_i) A_i \begin{pmatrix} [a_i^{(1)}]^2 \\ [b_i^{(1)}]^2 \end{pmatrix} + (1 - N_i) C_i \begin{pmatrix} a_i^{(1)} b_i^{(1)} \\ 0 \end{pmatrix}], \tag{19}$$

where

$$G_0 = \begin{pmatrix} 1 & 1 \\ n_0 & -n_0 \end{pmatrix}, \quad G_i = \begin{pmatrix} 1 & 1 \\ n_i^{(2)} & -n_i^{(2)} \end{pmatrix}, \quad B_i = \begin{pmatrix} 1 & 1 \\ 2n_i^{(1)} & -2n_i^{(1)} \end{pmatrix},$$
$$Q_i = \begin{pmatrix} e^{ik_i^{(2)} d_i} & 0 \\ 0 & e^{-ik_i^{(2)} d_i} \end{pmatrix}, \quad F_i = \begin{pmatrix} e^{2ik_i^{(1)} d_i} & 0 \\ 0 & e^{-2ik_i^{(1)} d_i} \end{pmatrix}. \tag{20}$$

Using the above recursive relation, we can straightforwardly obtain the SH electric field amplitudes at each layer in all structures. For instance, in the S_3 structure, by ignoring the second-order susceptibility of the SiO_2 and ZnS layers in comparison with MoS_2 monolayers, we have

$$\begin{aligned} \begin{pmatrix} E_t^{(2)+} \\ 0 \end{pmatrix} &= G_0^{-1} V_5^N G_0 \begin{pmatrix} 0 \\ E_r^{(2)-} \end{pmatrix} + \sum_{j=1}^{N} G_0^{-1} V_5^{N-j} \\ &\times \Bigg[(V_3 B_M F_M - V_4 B_M) A_M \begin{pmatrix} (a_{5j-3}^{(1)})^2 \\ (b_{5j-3}^{(1)})^2 \end{pmatrix} \\ &+ (V_3 - V_4) C_M \begin{pmatrix} a_{5j-3}^{(1)} b_{5j-3}^{(1)} \\ 0 \end{pmatrix} \\ &+ (B_M F_M - V_1 B_M) A_M \begin{pmatrix} (a_{5j}^{(1)})^2 \\ (b_{5j}^{(1)})^2 \end{pmatrix} + (1 - V_1) C_M \begin{pmatrix} a_{5j}^{(1)} b_{5j}^{(1)} \\ 0 \end{pmatrix} \Bigg], \end{aligned} \tag{21}$$

where $E_t^{(2)+}$ and $E_r^{(2)-}$ denote the forward and backward SH electric fields at the left and right sides, respectively, of different structures, $V_1 = N_M$, $V_2 = N_M N_S$, $V_3 = N_M N_S N_Z$, $V_4 = N_M N_S N_Z N_M$, and $V_5 = N_M N_S N_Z N_M N_S$.

Also, the theoretical results for the S_2, S_4, and S_5 structures are calculated in a similar way and we show the numerical results only. Forward and backward SHG efficiencies are defined as $\eta_F = \frac{|E_t^{(2)+}|^2}{|E_0^{(1)}|^2} \times 100$ and $\eta_B = \frac{|E_r^{(2)-}|^2}{|E_0^{(1)}|^2} \times 100$, respectively.

3. Numerical results and discussion

The amplitude of the incident FW of wavelength $\lambda = 810$ nm was set to $|E_0| = 1000$ V/m to establish the undepleted pump approximation in all simulations. We assume that the ZnS and SiO_2 layers have the same thickness ($d_Z = d_S = d$), which can be changed in all simulations, while the thickness of MoS_2 monolayers was fixed at $d_M = 0.65$ nm. The second-order susceptibility of MoS_2 monolayers was set as $\chi_M^{(2)} = 10^{-7}$ m/V and the second-order nonlinear optical coefficients of the ZnS and SiO_2 films were negligible in comparison with the MoS_2 coefficient [10,12–15].

We calculated the forward and backward SHG efficiencies for the same thickness of ZnS and SiO_2 films to obtain the optimal thickness with the highest efficiencies. Fig. 3 shows the results for different FPC structures in which all of them contain $M = 30$ MoS_2 monolayers. The building blocks of the S_2, S_3, S_4 and S_5 FPC structures are composed of one, two, three, and five MoS_2 layers, respectively. Fig. 3 demonstrates that the highest forward and backward efficiencies are 1.27×10^{-7} and 1.67×10^{-7}, respectively, in the S_2 structure, 1.29×10^{-6} and 2.2×10^{-6}, respectively, in the S_3 structure, 9.0×10^{-8} and 1.17×10^{-7}, respectively, in the S_4 structure, and 2.21×10^{-7} and 4.91×10^{-7}, respectively, in the S_5 structure. The results show that the highest efficiencies occur for the S_3 structure with respect to all structures. Also, the forward and backward SHG efficiencies in the S_3 structure are greater by more than one order of magnitude than those in the periodic S_2 structure.

As already mentioned, the MoS_2 monolayers play the role of an SH wave source in our structures. An SH wave generated in one layer travels to the other layers and can interfere with the new SH wave generated from secondary layers. The interference can be constructive if the phase difference between all SH waves is an integer multiple of the SH wavelength ($\Delta\varphi = m\lambda_{1/2}$, m is an integer and $\lambda_{1/2}$ is the SH wavelength). The main origin of the phase difference between two successive SHG sources (MoS_2 monolayers) comes from the optical path length of the SH wave between the two MoS_2 monolayers.

In the S_2 FPC, there are ZnS and SiO_2 layers between two successive MoS_2 layers, while in the other structures there are SiO_2 layers or SiO_2/ZnS bilayers between the nonlinear light source. Therefore, in S_i structures with $i \geq 3$, there are more geometrical parameters that can be tuned to obtain higher efficiencies. Also, Fig. 3 shows that the backward efficiency is higher than the forward efficiency in all structures. This occur since the material at the left-hand side of the MoS_2 nonlinear light source, SiO_2 layers, has the same or a lower refractive index than the right-hand-side materials (ZnS or SiO_2) at the SH wavelength ($n_Z(\lambda = 405\,\text{nm}) = 2.5434$, $n_S(\lambda = 405\,\text{nm}) = 1.5571$).

To fully understand the physics behind the enhancement of the SHG efficiencies, the transmission spectra of different engineered structures around the FW and SH wavelengths are demonstrated in Figs. 4 and 5 , respectively. The transmission spectrum of an FPC contains forbidden frequency regions called "pseudo band gaps," which are similar to the band gaps of a photonic crystal, while in the frequency regime outside these Fibonacci band gaps, the light waves are critically localized [22]. Figs. 4 and 5 show that the FW and SH wavelengths are both located at the photonic band gap edges for all engineered structures, where the density of electromagnetic fields is large and the group velocity is low. Therefore, the field amplitudes can be enhanced and the nonlinear interaction time becomes much longer.

In the next step, we investigated the optimal structure to obtain the highest SHG efficiencies by calculating η_F and η_B versus the number of segments. Fig. 6 shows the results, and shows the highest efficiencies for each structure are obtained with different numbers of segments. The highest forward SHG efficiency in the periodic S_2 photonic crystal is 1.98×10^{-6}, which is obtained with $N = 45$ segments ($M = 45$ MoS_2 monolayers). In the quasiperiodic FPCs, the highest forward SHG efficiencies are 1.95×10^{-4} ($N = 30$, $M = 60$), 4.30×10^{-4} ($N = 45$, $M = 135$), and 5.27×10^{-4} ($N = 15$, $M = 75$) in the S_3, S_4, and S_5 structures, respectively. The results show that the location of MoS_2 monolayers in 1D photonic crystals affects the SHG efficiencies. In quasiperiodic structures (S_i with $i = 3, 4, 5$) the SHG efficiencies are much greater than in the perfect periodic structure (S_2). Also, we need to use lower numbers of nonlinear MoS_2 monolayers in the S_3 structure ($M = 60$) with respect to the other quasiperiodic photonic crystals (S_4 ($M = 135$) and S_5 ($M = 75$)) to obtain the same order of SHG efficiency ($\eta_F \simeq 10^{-4}$). Furthermore, by our increasing the number of segments (N) in all structures, the overall thickness of the nonlinear MoS_2 light wave source was increased, which destroyed the phase matching conditions between SH waves and decreased the SHG efficiencies. This result is similar to that in our previous work [20]. The results shown in Fig. 6 and in Fig. 3 confirm that the S_3 FPC is the optimal structure to obtain the highest SHG efficiencies for the same number of MoS_2 nonlinear light wave sources.

Finally, we tried to control the propagation direction (forward or backward) of SH waves in our structures. To this end, we designed a distributed Bragg reflector (DBR) with high reflection coefficient at the SH wavelength ($\lambda = 405$ nm) and high transmittance at the FW wavelength ($\lambda = 810$ nm). In our design a 15-pair SiO_2/HfO_2 multilayer structure was integrated at the left side of all structures. The SiO_2 and HfO_2 thicknesses in the DBR were 70 and 48.5 nm, respectively. The refractive index of HfO_2 is described as follows [32]:

$$n_H(\lambda) = \sqrt{1 + \frac{1.9558\lambda^2}{\lambda^2 - 0.15494} + \frac{1.345\lambda^2}{\lambda^2 - 0.0634} + \frac{10.41\lambda^2}{\lambda^2 - 27.12^2}}, \tag{22}$$

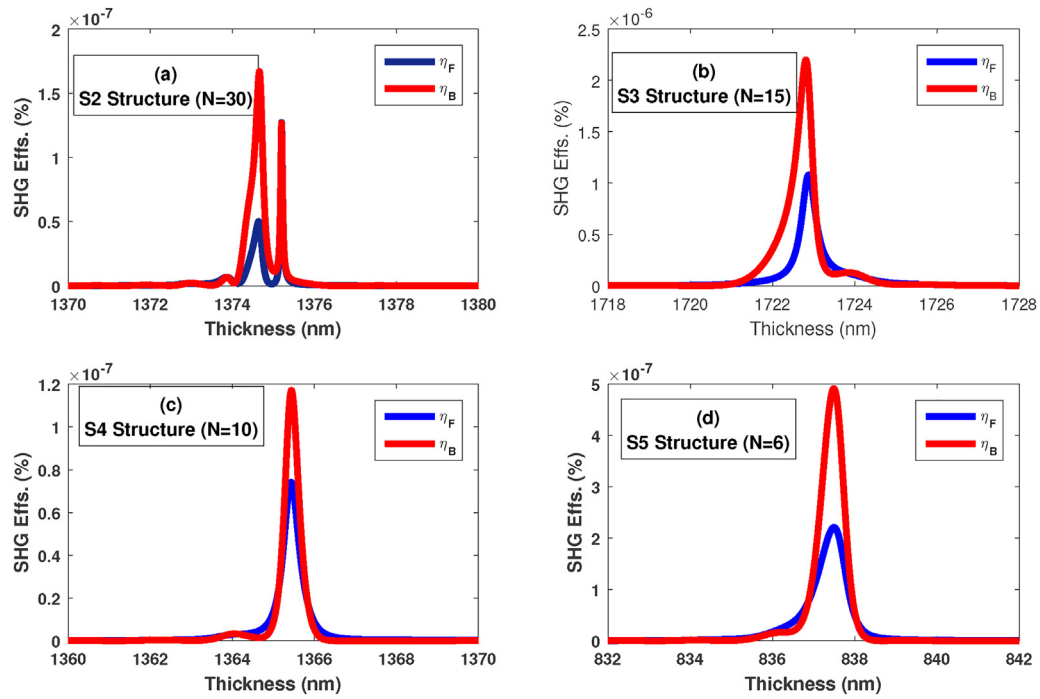

Fig. 3. Forward and backward second-harmonic generation (SHG) efficiencies versus the same thickness of ZnS and SiO_2 layers for (a) the S_2 structure ($N = 30$), (b) the S_3 structure ($N = 15$), (c) the S_4 structure ($N = 10$), and (d) the S_5 structure ($N = 6$).

where the wavelength is in micrometers. The reflectance of the DBR is depicted in Fig. 7, which shows that the SH wavelength is located in the band gap of the DBR, while the reflection of the FW is negligible. We used this mirror at the left side of our structures to control and to reduce the backward SH waves.

Fig. 8 is similar to Fig. 3 but the DBR is located at the left side of the structures. The results show that in the presence of a Bragg mirror the backward SHG efficiencies are decreased by up to three orders of magnitude and the forward efficiencies are increased by up to one order of magnitude. Therefore, it is possible to control the propagation direction of the generated second-harmonic wave by use of a subtly designed Bragg mirror.

4. Conclusion

The efficiencies of SHG from different engineered 1D FPCs

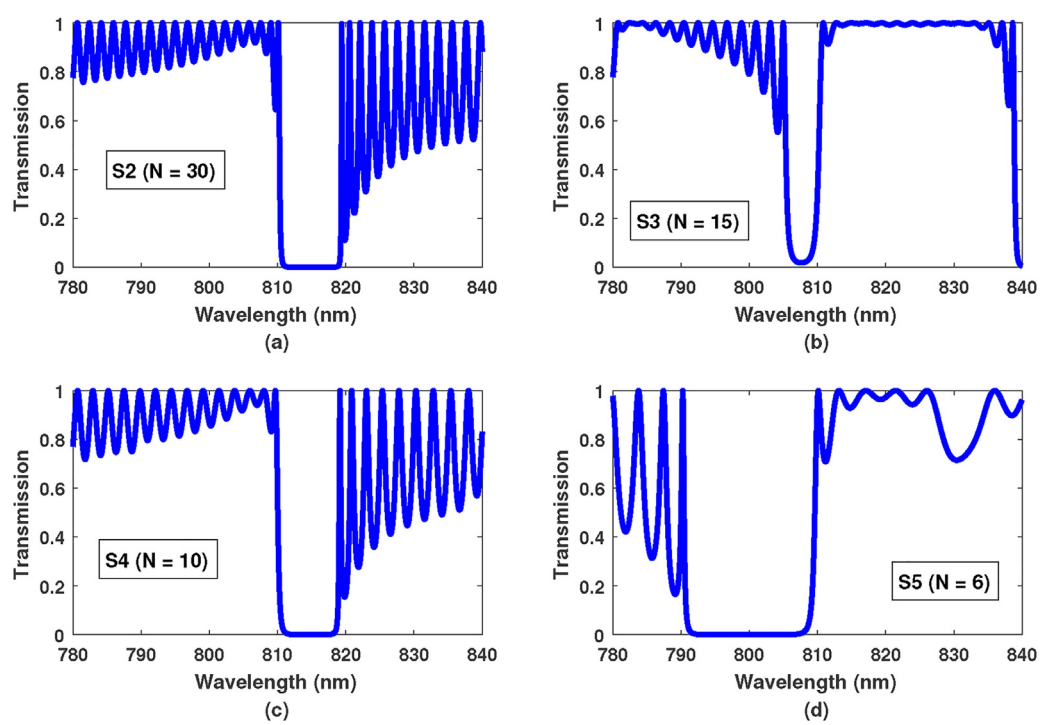

Fig. 4. Transmission spectra around the fundamental wave wavelength in a one-dimensional nonlinear photonic crystal: (a) S_2 structure ($N = 30$), (b) S_3 structure ($N = 15$), (c) S_4 structure ($N = 10$), and (d) S_5 structure ($N = 6$).

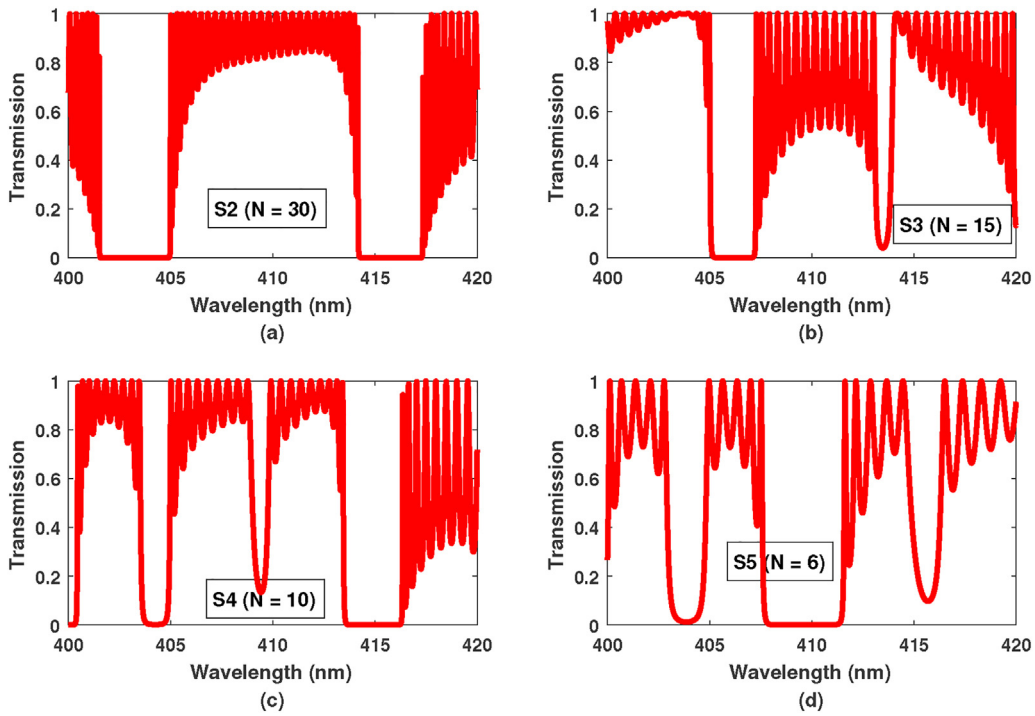

Fig. 5. Transmission spectra around the second-harmonic wavelength in a one-dimensional nonlinear photonic crystal: (a) S_2 structure ($N = 30$), (b) S_3 structure ($N = 15$), (c) S_4 structure ($N = 10$), and (d) S_5 structure ($N = 6$).

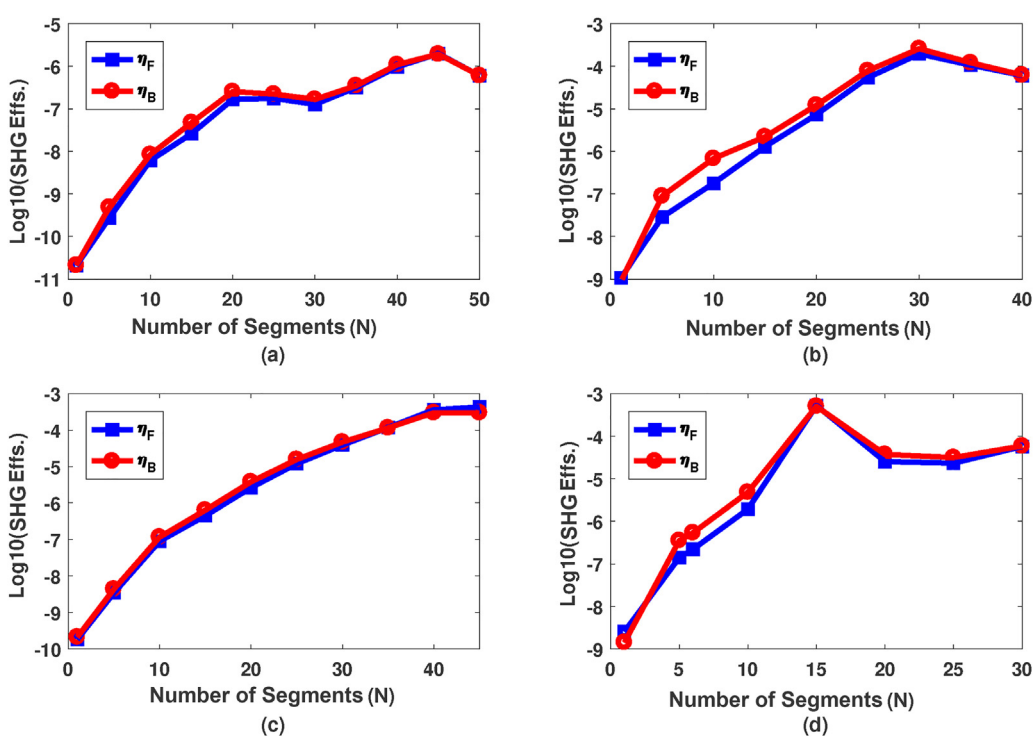

Fig. 6. Forward and backward second-harmonic generation (SHG) efficiencies versus the number of segments (N) on a logarithmic scale for a one-dimensional nonlinear photonic crystal: (a) S_2 structure, (b) S_3 structure, (c) S_4 structure, and (d) S_5 structure.

containing MoS_2 monolayers, as 2D TMD structures, ZnS, and SiO_2 films were calculated. The transfer matrix method in the undepleted pump approximation was used to calculate the forward and backward SHG efficiencies. The thicknesses of the ZnS and SiO_2 films were changed to obtain the maximum frequency conversion in different structures. Tuning the thickness causes the SH waves that are generated in each MoS_2 monolayer to interfere constructively, and the FW and SH wavelengths are both located at the photonic pseudo band gap edges, where the light localization is enhances and the nonlinear interaction time is increased. Our results show that the S_3 FPC is the optimal structure among the first four engineered FPCs with regard to the highest SHG efficiencies for the same number of MoS_2 nonlinear light wave sources. Also, we used a Bragg mirror at one side of our structures to control the propagation direction of the generated SH waves and to

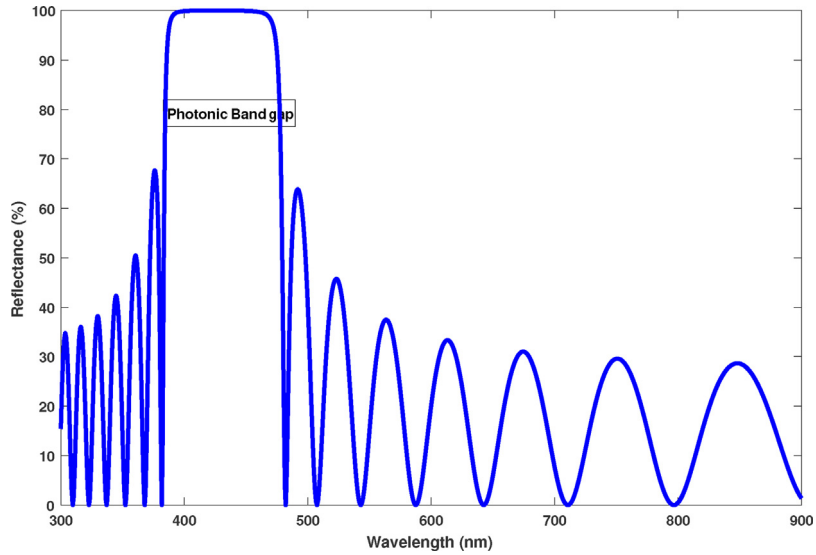

Fig. 7. The reflectance of the distributed Bragg reflector containing a 15-pair SiO_2/HfO_2 multilayer structure.

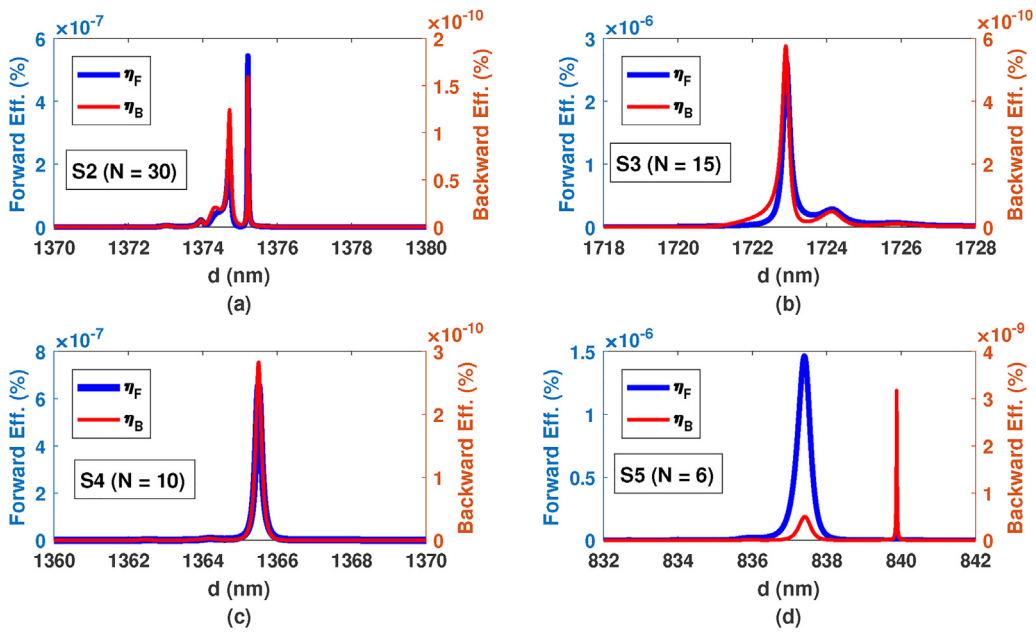

Fig. 8. Forward and backward seond-harmonic generation efficiencies versus the same thickness of ZnS and SiO_2 layers in the presence of a distributed Bragg reflector at the left side of all structures for (a) the S_2 structure ($N = 30$), (b) the S_3 structure ($N = 15$), (c) the S_4 structure ($N = 10$), and (d) the S_5 structure ($N = 6$).

decrease the backward waves, which led to enhancement of the forward waves. This study can be extended to higher FPC generations and other quasiperiodic photonic crystals.

Acknowledgment

The authors thank E. Vazifedoust for his comments on the manuscript.

References

[1] A. Autere, H. Jussila, Y. Dai, Y. Wang, H. Lipsanen, Z. Sun, Nonlinear optics with 2D layered materials, Adv. Mater. 81 (2018) 1705963.
[2] K.F. Mak, J. Shan, Photonics and optoelectronics of 2D semiconductor transition metal dichalcogenides, Nat. Photon. 10 (2016) 216–226.
[3] X. Hong, J. Kim, S.F. Shi, Y. Zhang, C. Jin, Y. Sun, S. Tongay, J. Wu, Y. Zhang, F. Wang, Ultrafast charge transfer in atomically thin MoS_2/WS_2 heterostructures, Nat. Nanotechnol. 9 (2014) 682–686.
[4] J.T. Liu, H. Tong, Z.H. Wu, J.B. Huang, Y.S. Zhou, Greatly enhanced light emission of MoS_2 using photonic crystal heterojunction, Sci. Rep. 7 (2017) 16391.
[5] Q.H. Wang, K. Kalantar-zadeh, A. Kis, J.N. Coleman, M.S. Strano, Electronics and optoelectronics of two-dimensional transition metal dichalcogenides, Nat. Nanotechnol. 7 (2012) 699–712.
[6] K.F. Mak, C. Lee, J. Hone, J. Shan, T.F. Heinz, Atomically thin MoS_2: a new direct-gap semiconductor, Phys. Rev. Lett. 105 (2010) 136805.
[7] H. Zeng, et al., Optical signature of symmetry variations and spin-valley coupling in atomically thin tungsten dichalcogenides, Sci. Rep. 3 (2013) 1608.
[8] X.B. Yin, Z.L. Ye, D.A. Chenet, Y. Ye, K. O'Brien, et al., Edge nonlinear optics on a MoS_2 atomic monolayer, Science 344 (2014) 488–490.
[9] G. Wang, X. Marie, I. Gerber, T. Amand, D. Lagarde, et al., Giant enhancement of the optical second-harmonic emission of WSe_2 monolayers by laser excitation at exciton resonances, Phys. Rev. Lett. 114 (2015) 097403.
[10] N. Kumar, S. Najmaei, Q.N. Cui, F. Ceballos, P.M. Ajayan, et al., Second harmonic microscopy of monolayer MoS_2, Phys. Rev. B 87 (2013) 161403.
[11] C. Janisch, Y.X. Wang, D. Ma, N. Mehta, A.L. Elias, et al., Extraordinary second harmonic generation in tungsten disulfide monolayers, Sci. Rep. 4 (2014) 5530.
[12] L.M. Malard, T.V. Alencar, A.P.M. Barboza, K.M. Mak, A.M.D. Paula, Observation of intense second harmonic generation from MoS_2 atomic crystals, Phys. Rev. B 87 (2013) 201401.
[13] J.H. Zeng, M.H. Yuan, W.G. Yuan, Q.F. Dai, H.H. Fan, et al., Enhanced second harmonic generation of MoS_2 layers on a thin gold film, Nanoscale 7 (2015)

13547–13553.
[14] J.K. Day, M.H. Chung, Y.H. Lee, V.M. Menon, Microcavity enhanced second harmonic generation in 2D MoS_2, Opt. Mater. Express 6 (2016) 2360–2365.
[15] Y. Li, et al., Probing symmetry properties of few-layer MoS_2 and h-BN by optical second-harmonic generation, Nano Lett. 13 (2013) 3329–3333.
[16] B. Mukherjee, F. Tseng, D. Gunlycke, K.K. Amara, G. Eda, E. Simsek, Complex electrical permittivity of the monolayer molybdenum disulfide (MoS_2) in near UV and visible, Opt. Mater. Express 5 (2015) 447.
[17] C. Yim, M. O'Brien, N. McEvoy, S. Winters, I. Mirza, J.G. Lunney, G.S. Duesberg, Investigation of the optical properties of MoS_2 thin films using spectroscopic ellipsometry, Appl. Phys. Lett. 104 (2014) 103114.
[18] H. Zhang, Y. Ma, Y. Wan, X. Rong, Z. Xie, W. Wang, L. Dai, Measuring the refractive index of highly crystalline monolayer MoS_2 with high confidence, Sci. Rep. 5 (2015) 8440.
[19] H. Chen, V. Corboliou, A.S. Solntsev, D.Y. Choi, M.A. Vincenti, D. De Ceglia, C.D. Angelis, Y. Lu, D.N. Neshev, Enhanced second-harmonic generation from two-dimensional $MoSe_2$ on a silicon waveguide, Light: Sci. Appl. 6 (2017) 17060.
[20] M. Khani, M. Khazaei Nezhad, H. Rastegar Moghaddam Rezaeiun, Giant enhancement of second harmonic generation efficiency from MoS_2 mono layers embedded in 1D photonic crystals, Eur. Phys. J. Plus 133 (2018) 338.
[21] Y.C. Lin, C.H. Tsou, W.J. Hsueh, Ultra-slow light in one-dimensional Cantor photonic crystals, Opt. Lett. 43 (2018) 4120.
[22] L. Dal Negro, J.H. Yi, V. Nguyen, Y. Yi, J. Michel, L.C. Kimerling, Spectrally enhanced light emission from aperiodic photonic structures, Appl. Phys. Lett. 86 (2005) 261905.
[23] E. Macia, Exploiting aperiodic designs in nanophotonic devices, Rep. Prog. Phys. 75 (2012) 036502.
[24] J.J. Li, Z.Y. Li, D.Z. Zhang, Second harmonic generation in one-dimensional nonlinear photonic crystals solved by the transfer matrix method, Phys. Rev. E 75 (2007) 056606.
[25] J. Li, Z. Li, Y. Sheng, D. Zhang, Giant enhancement of second harmonic generation in poled ferroelectric crystals, Appl. Phys. Lett. 91 (2007) 022903.
[26] M.L. Ren, Z.Y. Li, Enhanced nonlinear frequency conversion in defective nonlinear photonic crystals with designed polarization distribution, J. Opt. Soc. Am. B 27 (2010) 1551.
[27] S.M. Hamidi, T. Parvini, M.M. Tehranchi, Efficient second harmonic conversion efficiency through one-dimensional coupled resonator poled nonlinear optical waveguide, Appl. Phys. A 111 (2013) 525.
[29] G. Ghosh, Dispersion-equation coefficients for the refractive index and birefringence of calcite and quartz crystals, Opt. Commun. 163 (1999) 95–102.
[30] C.A. Klein, Room-temperature dispersion equations for cubic zinc sulfide, Appl. Opt. 25 (1986) 1873–1875.
[31] I. Sharma, B.R. Mehta, Enhanced charge separation at 2D MoS_2/ZnS heterojunction: KPFM based study of interface photovoltage, Appl. Phys. Lett. 110 (2017) 061602.
[32] D.L. Wood, K. Nassau, T.Y. Kometani, D.L. Nash, Optical properties of cubic hafnia stabilized with yttria, Appl. Opt. 29 (1990) 604–607.